

Measurement of thermal parameter and Reynolds number effects on cavitation instability onset in a turbopump inducer

Original article

Article history:

Accepted: 24 June 2017

Published: 9 August 2017

This paper is the updated version of a paper originally presented at the 1st Global Power and Propulsion Forum, GPPF 2017, in Zurich, Jan 16-18 2017



*Correspondence:

JK: kimjonah@snu.ac.kr

Peer review:

Single blind

Copyright:

© 2017 Kim and Song. © This is an open access article distributed under the Creative Commons Attribution License (CC-BY 4.0), which permits unrestricted use, distribution, and reproduction in any medium, provided the original work is properly cited and its authors credited.

Keywords:

Reynolds number; thermal effect; turbopump inducer; cavitation instability

Citation:

Kim J. and Song S. J. (2017). Measurement of thermal parameter and Reynolds number effects on cavitation instability onset in a turbopump inducer. *Journal of the Global Power and Propulsion Society*. 1: 157–170. <https://doi.org/10.22261/H5DYU3>

Junho Kim*, Seung Jin Song

Department of Mechanical Engineering, Seoul National University Seoul 151-744, Republic of Korea

Abstract

This study experimentally examines how the non-dimensional thermal parameter and Reynolds number affect cavitation instability onset in a turbopump inducer using water. Based on the time-resolved static pressure measured at the inlet of the turbopump inducer, the onset cavitation number of rotating cavitation has been determined for varying Reynolds number and non-dimensional thermal parameter values. Increasing non-dimensional thermal parameter suppresses rotating cavitation and causes a monotonic decrease in the rotating cavitation onset cavitation number. At low non-dimensional thermal parameter values (e.g., 0.0125), the onset cavitation number is independent of the Reynolds number. However, at higher values of the non-dimensional thermal parameter (e.g., higher than 0.0537), the onset cavitation number increases with increasing Reynolds number. Thus, the Reynolds number promotes rotating cavitation onset. This study provides the first assessment of the independent effects of the non-dimensional thermal parameter and Reynolds number.

Introduction

For a liquid rocket engine, turbopumps supply liquid oxidizer and fuel to the combustion chamber at high pressure. Turbopumps rotate at high speeds to reduce the rocket engine weight and achieve high power densities. Such requirement leads to cavitation in turbopumps. Therefore, to inhibit cavitation in the impeller, an axial type inducer is installed upstream of the turbopump. However, the inducer itself can suffer from cavitation. When the inducer cavitation becomes severe, its head coefficient, ψ , is decreased. Critical cavitation number (defined to be the cavitation number at which the head coefficient value decreases to 97 % of the nominal value) is used to signify the head coefficient degradation. Inducer cavitation can also cause hydraulic instabilities- rotating cavitation, asymmetric attached cavitation, and cavitation surge (Tsujiimoto et al., 1997). The onset cavitation number is used to quantify the beginning of cavitation instability.



In cryogenic fluids or hot water, the temperature and vapor pressure within the cavitation bubbles are decreased due to the latent heat absorption by the bubbles from the liquid during the vaporization process. This phenomenon is referred to as the “thermal effect.” As the liquid temperature increases, the thermal effect is enhanced, and cavitation bubble growth is suppressed (Brennen, 1994). Ruggeri and Moore (1969) measured cavitation performance for pumps and inducers in liquid hydrogen. The critical cavitation number decreased with increasing liquid temperature or decreasing rotational speed. Kikuta et al. (2008) found that the critical cavitation number and cavitation region length were decreased as the liquid nitrogen temperature was increased. Torre et al. (2011) found that the critical cavitation number was reduced at high water temperatures.

Franc et al. (2001) observed the variations in cavitation region length at the inducer leading edge and the onset of cavitation instabilities with changes in the liquid (refrigerant R-114) temperature and rotational speed. As R-114 temperature increased, the leading edge cavitation region was shortened and rotating cavitation occurred at lower cavitation numbers. In R-114 (in which the thermal effect existed), the cavitation region was lengthened as the rotational speed increased, but the cavitation region length was insensitive to the rotational speed in cold water (in which the thermal effect was negligible).

Yoshida et al. (2007, 2009) investigated cavitation instabilities at different liquid nitrogen temperatures. They found the followings. First, rotating cavitation occurred at the same length of tip vortex leakage cavitation region regardless of temperature. Second, the onset cavitation numbers of rotating cavitation and asymmetric attached cavitation were decreased as the temperature of liquid nitrogen increased. Finally shaft vibration and rotating cavitation amplitudes were reduced at high liquid temperatures.

Alternatively, to quantify such thermal effects, two parameters have been suggested. Brennen (1994) suggested a dimensional thermal parameter, Σ ($\text{m/s}^{3/2}$), from the Rayleigh-Plesset equation. Σ represents the amount of vapor pressure depression due to the thermal effect in a fluid (Equation 1).

$$\Sigma = \frac{(\rho_v L)^2}{\rho_l^2 C_{pl} T_\infty \sqrt{\alpha_l}} \quad (1)$$

For cavitation in fluid machines, Franc et al. (2004) derived a non-dimensional thermal parameter, Σ^* by nondimensionalizing the Rayleigh-Plesset equation (Equation 2). For simplicity, they assumed inviscid flow.

$$\bar{R} \frac{d^2 \bar{R}}{d\bar{x}^2} + \frac{3}{2} \left(\frac{d\bar{R}}{d\bar{x}} \right)^2 + \Sigma^* \sqrt{\bar{x}} \frac{d\bar{R}}{d\bar{x}} = - \frac{C_p + \sigma}{2} \quad (2)$$

In Equation 2, $\Sigma^* = \Sigma \sqrt{C/U^3}$ in which the bubble radius (R) and the distance (x) have been non-dimensionalized by the characteristic length C . C_p is the pressure coefficient, and σ is the cavitation number. In addition to the fluid properties of Σ , Σ^* incorporates the characteristic length (C) and reference velocity (U) of the pump representing the amount of the thermal effect on cavitation in fluid machines. In Equation 1, as the temperature of the working fluid increases, the vapor density increases faster than the increase in the temperature. Thus, Σ is increased. According to Equation 2, Σ^* is increased as the liquid temperature increases or the reference velocity decreases. In actual rocket engines using liquid oxygen, Σ^* ranges from 1.5 to 30 depending on the size and rotational speed of the inducer.

Watanabe et al. (2007, 2008) independently derived the non-dimensional thermal parameter Σ^* in their analysis of an inducer cascade and found that increasing Σ^* suppressed the onset of cavitation instabilities. Kikuta et al. (2009) investigated the rotational speed effects using Σ^* in liquid nitrogen. The cavitation region length and critical cavitation number both decreased as Σ^* increased.

Hot water can be used as a surrogate test fluid for cryogenic oxidizer or propellant when it satisfies the similarity requirement in terms of the non-dimensional thermal parameter. Ehrlich and Murdock (2015) derived their DB parameter, which is a reciprocal of Σ^* , and they matched their DB value in water with that of liquid oxygen. In water, they found that decreasing DB completely suppressed rotating cavitation. Kim and Song (2016) investigated rotating cavitation onset trends for varying Σ^* by changing the water temperature at a given rotational speed. The onset cavitation number decreased

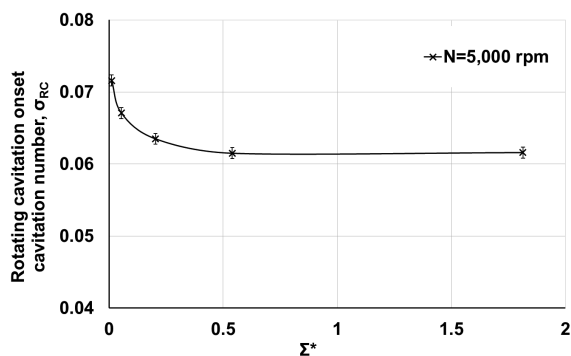


Figure 1. The rotating cavitation onset cavitation number versus the non-dimensional thermal parameter at 5,000 rpm and $\varphi/\varphi_d = 1.0$ (Kim and Song, 2016).

as Σ^* was increased for $\Sigma^* < 0.54$. However, for $\Sigma^* \geq 0.54$, the onset cavitation number remained constant as Σ^* was increased (Figure 1).

Previous researchers investigated the thermal effect on cavitating inducers by varying either the liquid temperature or rotational speed, but they did not consider viscous effects. However, when either the liquid temperature or rotational speed is changed, not only Σ^* but also the Reynolds number ($Re = 2\rho_l r \Omega^2 / \mu_l$) is simultaneously changed. In Kim and Song (2016), as Σ^* was increased from 0.0116 to 1.80, the Reynolds number ranged from 2.6×10^6 to 6.4×10^6 as well. It indicates that Reynolds number possibly affects the occurrence of rotating cavitation. Yet, the individual effects of Σ^* and Re on the cavitation instability onset have not been examined.

Therefore, the research objective of this study is to measure and understand the individual effects of Σ^* and Re on the onset of cavitation instability in a turbopump inducer.

Non-dimensional parameters

To identify the non-dimensional parameters governing cavitation growth in an inducer, the Rayleigh-Plesset equation for bubble dynamics is presented in Equation 3 (Plesset and Prosperetti, 1977).

$$R \frac{d^2 R}{dt^2} + \frac{3}{2} \left(\frac{dR}{dt} \right)^2 + \Sigma \frac{dR}{dt} \sqrt{t} + \frac{4\mu_L}{\rho_L} \frac{dR}{dt} + \frac{2S}{R} - \frac{p_{G0}}{\rho_L} \left(\frac{R_0}{R} \right)^{3k} = \frac{p_v(T_\infty) - p_\infty}{\rho_L} \quad (3)$$

Following Franc et al. (2004), time has been normalized by x/U where x is the distance along the streamline followed by the bubble; U is the inducer blade tip rotational speed; and C is the inducer radius. Surface tension (S) and non-condensable gas effects (p_{G0}) are negligible after the initial stage of bubble formation (Brennen, 1995). The resulting non-dimensional Rayleigh-Plesset equation is then:

$$\bar{R} \frac{d^2 \bar{R}}{d\bar{x}^2} + \frac{3}{2} \left(\frac{d\bar{R}}{d\bar{x}} \right)^2 + \left(\Sigma^* \sqrt{\bar{x}} + \frac{4}{Re\bar{R}} \right) \frac{d\bar{R}}{d\bar{x}} = - \frac{Cp + \sigma}{2} \quad (4)$$

In Equation 4, Σ^* and Re are the two non-dimensional parameters which affect cavitation bubble growth. Increasing liquid temperature increases both Σ^* and Re . Increasing inducer blade tip velocity increases Re but decreases Σ^* .

Experimental apparatus and instrumentation

Figure 2 shows a schematic of the turbopump inducer water test facility at Seoul National University (Kim and Song, 2016). The test facility has been designed to measure cavitating and non-cavitating inducer/pump performance over a wide range of operating conditions. The closed loop test facility includes a water tank, test section, flow straightener, control valve, and booster pump. A vacuum pump and compressed air supply pipe are connected to the water tank to control pressure. To adjust the water temperature, a 20-kW electrical heater has been employed in the water tank. The filtered water from the tank is circulated in the direction shown in Figure 2. Downstream of the collector, a flow straightener is located upstream of the flow meter for accurate flow rate measurement, and the control valve sets the flow rate. Farther downstream, the booster pump maintains a constant flow rate under cavitating conditions. Elastic couplings have been installed at the exit of the water tank and collector for alignment and vibration control. Rotating parts are composed of the

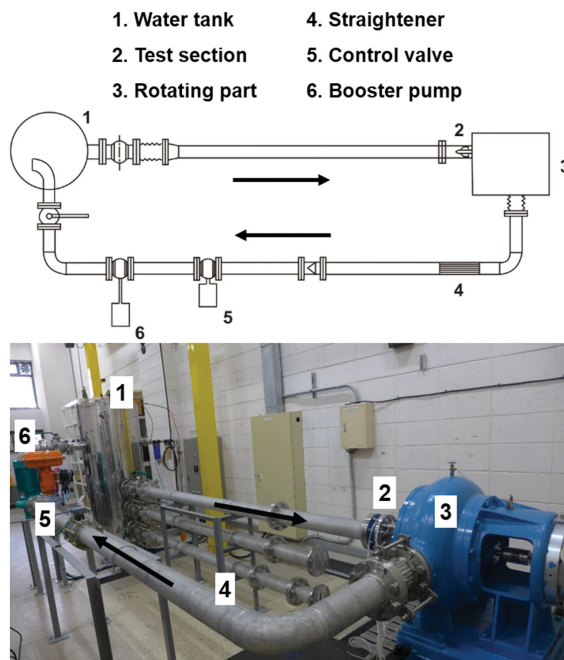


Figure 2. SNU turbopump inducer experimental facility.

± 0.000422 , and ± 0.000759 , respectively. All of the data presented in the paper have been acquired at the design flow rate condition.

The test inducer (Figure 4) has been designed by the Korea Aerospace Research Institute (KARI), and its specifications are summarized in Table 1. The inducer has a high solidity and moderate blade tip angle at the inlet (Choi et al., 2006).

Experimental results and discussion

Cavitation instabilities

Fast Fourier Transform analysis and the cross-correlation of signals from two unsteady pressure transducers have been used to determine cavitation instability characteristics. Figure 5 shows the power spectral density plots of the unsteady pressure transducer signals for varying cavitation number (Kim and Song, 2016). Three dominant peaks at $f/\Omega = 3.0$ ($\sigma > 0.072$), 1.14 ($0.053 < \sigma < 0.072$), and 1.0 ($\sigma < 0.053$) are visible. According to Kim and Song (2016), the peaks at $f/\Omega = 3.0$, 1.14, and 1.0 correspond to blade passing frequency, rotating cavitation, and asymmetric attached cavitation, respectively.

Rotating cavitation results in uneven cavitation regions rotating at a speed faster (super-synchronous) than the inducer rotational speed in the same direction. Thus, the frequency of rotating cavitation is $f/\Omega = 1.14$ in the tested inducer (Kim and Song, 2016). In the present study, the onset cavitation number of rotating

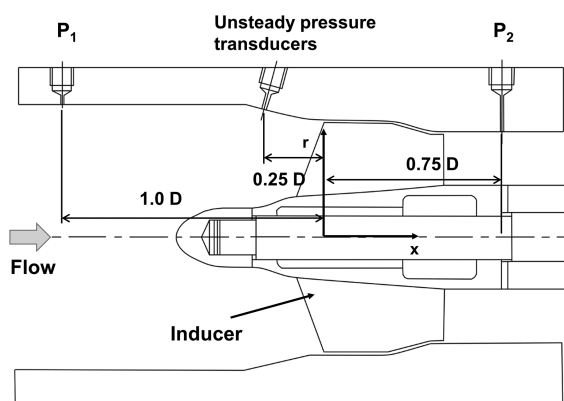


Figure 3. Test section schematic.

test inducer, shaft, and motor. A 60-kW motor drives the inducer at rotational speeds of up to 10,000 rpm. The rotational speed of the motor is controlled to within ± 1 rpm by a variable frequency drive.

Figure 3 shows the test section instrumentation locations (Kim and Song, 2016). Eight and four static pressure taps at $x/D = -1.0$ (P_1) and 0.75 (P_2) have been used to measure the inducer static head coefficient and cavitation number. Eight unsteady pressure transducers with an accuracy of 0.1 % of the full scale value (350 kPa) and 400 kHz frequency response have been installed at $x/D = -0.25$ to detect cavitation instabilities. Unsteady pressure signals have been sampled at 50 kHz for 1 second. Bulk water temperature has been maintained to within ± 0.1 K during the test. The mean flow rate has been measured downstream of the flow straightener using an electro-magnetic flow meter with an accuracy of 0.25% of the full scale value (20 kg/s). The uncertainties of the head coefficient (ψ), flow coefficient (Φ) and cavitation number (σ) with a 95% confidence interval are ± 0.00398 ,



Figure 4. Test inducer.

cavitation (σ_{RC}) is defined to be the cavitation number at which the amplitude of the rotating cavitation frequency increases to five times its steady state amplitude. Repeatability for the onset of rotating cavitation has been confirmed by three separate tests, and σ_{RC} is repeatable to within 0.7% at the design flow coefficient.

Non-dimensional thermal parameter effects for constant Reynolds number

To investigate the effects of Σ^* for constant Reynolds number, Σ^* has been varied from 0.0227 to 1.55 while Re has been held constant at 4.15×10^6 . The test conditions are summarized in Table 2. From heat transfer analysis (Bergman and Incropera, 2011), the temperature difference between the bulk water and wall varies from 0.04 K (308 K and 6,400 rpm) to 0.09 K (347 K and 3,500 rpm). The analysis procedure is described in the Appendix. The value of $\Sigma^* = 1.59$ is similar to $\Sigma^* = 1.81$ of the KARI liquid oxygen (LOX) inducer under the actual operating conditions (87 K and 20,000 rpm).

Figure 6 presents the power spectral density plots of the inlet unsteady pressure fluctuations for Σ^* ranging from 0.0229 to 1.59 at $Re = 4.15 \times 10^6$. The arrows indicate the onset cavitation number of rotating cavitation, σ_{RC} . The onset cavitation number and magnitude of the rotating cavitation (RC) at $f/\Omega = 1.14$ are decreased as Σ^* increases. Figure 7 shows the σ_{RC} plotted versus Σ^* . σ_{RC} monotonically decreases by 21% as Σ^* is increased from 0.0229 to 1.59. High-speed camera flow visualization qualitatively confirms this trend. Figure 8a shows the cavitation region on an inducer blade for $\Sigma^* = 0.0229$, and Figure 8b shows the same blade for $\Sigma^* = 1.59$ at $\sigma = 0.081$ and $Re = 4.15 \times 10^6$. The cavitation region for $\Sigma^* = 1.59$ is visibly smaller than that for $\Sigma^* = 0.0229$. According to Horiguchi et al. (2000), the onset of rotating cavitation depends on the length of the cavitation region. Thus, the

Table 1. Design characteristics of the test inducer.

| Item | Value |
|---------------------------------------|--------------------------------------|
| Diameter (D) | 0.094 m |
| Design flow coefficient (Φ_d) | 0.096 |
| Blade number | 3 |
| Solidity at tip | 2.7 |
| Blade tip angle | |
| Inlet (β_{1t}) | 9.6 deg |
| Outlet (β_{2t}) | 15.0 deg |
| Non-dimensional tip clearance (c/D) | 0.0106 |
| Angle variation on line normal to hub | $\tan(\beta) = (r_t/r)\tan(\beta_t)$ |

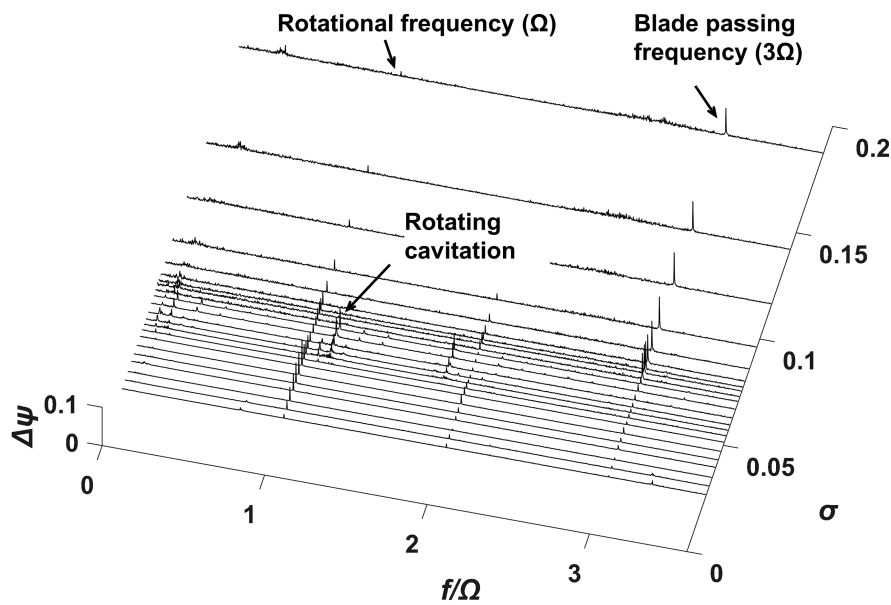


Figure 5. The power spectral density of inducer inlet pressure fluctuations ($\varphi/\varphi_d = 1.0$, $\Sigma^* = 0.0116$, $Re = 2.58 \times 10^6$ [$T_\infty = 298$ K and 5,000 rpm]).

visualization data are qualitatively consistent with the unsteady pressure data and confirm that increasing Σ^* suppresses the rotating cavitation onset.

Ruggeri and Moore (1969) defined the minimum cavitation number, σ_{min} , which determines the cavitation bubble growth by considering the thermal effect (Equation 5) as

$$\sigma_{min} = \frac{p_\infty - p_{v,min}}{\frac{1}{2}\rho_l U^2} = \sigma + \frac{p_{v,\infty} - p_{v,min}}{\frac{1}{2}\rho_l U^2} = \sigma + \frac{\Delta p_v}{\frac{1}{2}\rho_l U^2} \quad (5)$$

where $p_{v,min}$ is the minimum vapor pressure within the cavitation bubble. The minimum cavitation number is the sum of the cavitation number (σ) and the vapor pressure depression (Δp_v) normalized by the dynamic head ($\frac{1}{2}\rho_l U^2$). As Σ^* is increased, Δp_v of the cavitation bubbles is increased, and σ_{min} increases. Thus, increasing Σ^* inhibits rotating cavitation onset.

Table 2. Test conditions for thermal parameter effects.

| | Temperature [K] | Rotational speed [rpm] | Σ [$m/s^{3/2}$] | Reynolds number | $\Sigma^* = \Sigma\sqrt{C/U^3}$ |
|-------|-----------------|------------------------|--------------------------|--------------------|---------------------------------|
| Water | 308 | 6,400 | 1.87×10^1 | 4.14×10^6 | 2.29×10^{-2} |
| | 313 | 6,000 | 3.14×10^1 | 4.18×10^6 | 4.21×10^{-1} |
| | 323 | 5,000 | 7.60×10^1 | 4.18×10^6 | 1.35×10^{-1} |
| | 337 | 4,000 | 2.43×10^2 | 4.13×10^6 | 6.03×10^{-1} |
| | 347 | 3,500 | 5.24×10^2 | 4.13×10^6 | 1.59 |
| LOX | 86.6 | 20,000 | 8.21×10^3 | 5.04×10^7 | 1.82 |

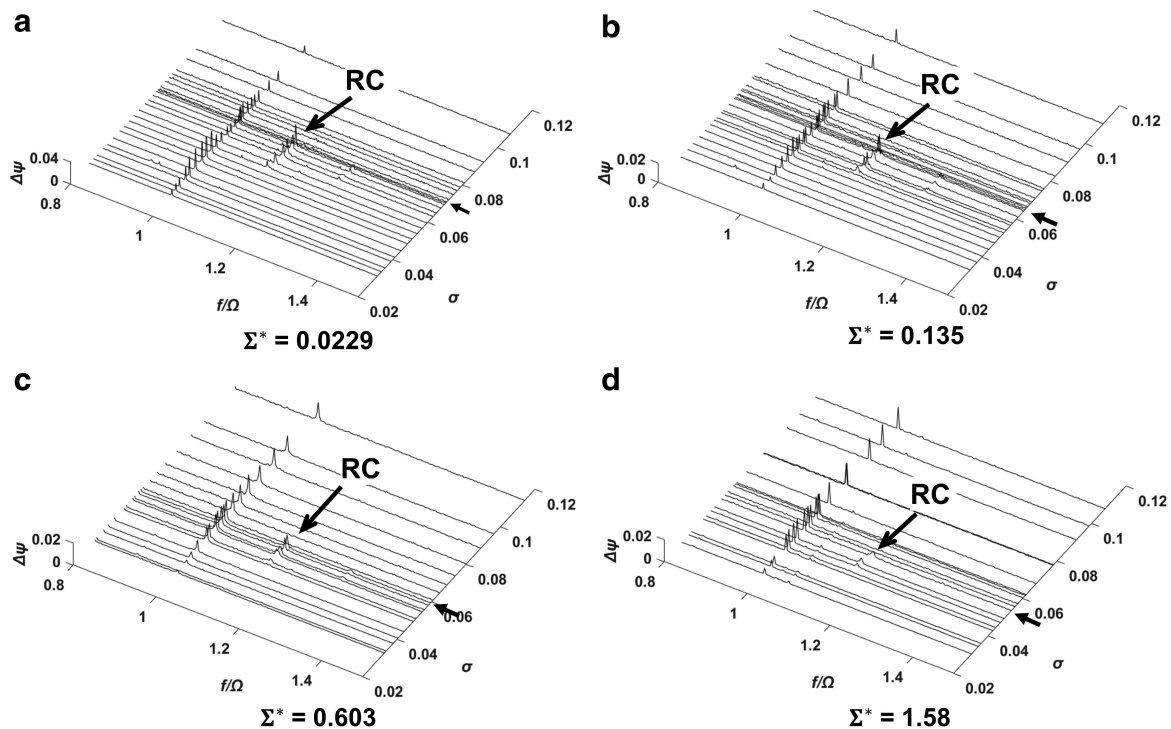


Figure 6. The power spectral density of unsteady pressure fluctuation at various non-dimensional thermal parameter at $Re = 4.15 \times 10^6$ and $\varphi/\varphi_d = 1.0$ for $\Sigma^* = 0.0229$ (a), 0.135 (b), 0.603 (c), 1.58 (d).

Reynolds number effects for constant non-dimensional thermal parameter

Table 3 lists the test conditions for Re effects. Figure 9 shows the power spectral density plots at $Re = 2.30 \times 10^6$ (Figure 9a) and 3.17×10^6 (Figure 9b) for $\Sigma^* = 0.0125$. Figure 10 shows the corresponding data at $Re = 4.81 \times 10^6$ (Figure 10a) and 6.84×10^6 (Figure 10b) for $\Sigma^* = 1.26$. The arrows indicate σ_{RC} . For $\Sigma^* = 0.0125$, σ_{RC} remains constant as Re increases. For $\Sigma^* = 1.26$, σ_{RC} at $Re = 6.84 \times 10^6$ is higher than that at $Re = 4.81 \times 10^6$.

The dependence of σ_{RC} on Re for various values of Σ^* is presented in Figure 11. For $\Sigma^* = 0.0125$, σ_{RC} is independent of Re . On the other hand, for $\Sigma^* \geq 0.0537$, σ_{RC} increases with increasing Re , and such Re effects (e.g., $\frac{\partial(\sigma_{RC})}{\partial(Re)}$) become stronger as Σ^* increases. Visualization of the cavitation on

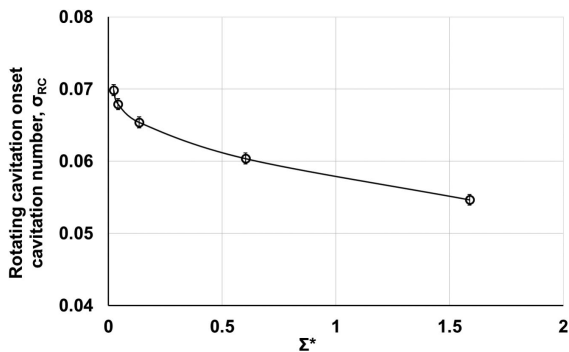


Figure 7. The rotating cavitation onset cavitation number versus the non-dimensional thermal parameter comparing at $Re = 4.15 \times 10^6$ and $\varphi/\varphi_d = 1.0$.

inducer blades qualitatively confirms such Re effects. Figure 12 shows the inducer blade cavitation at $Re = 2.30 \times 10^6$ (Figure 12a) and 3.17×10^6 (Figure 12b) for $\Sigma^* = 0.0125$. For $\Sigma^* = 0.0125$, the length of the inducer blade cavitation region is not affected by the Re change. For sufficiently low Σ^* (e.g., 0.0125), where the thermal effect is negligible [17], the vapor pressure depression is also negligible ($\Delta p_v \approx 0$). Therefore, σ_{min} (Equation 5) and σ_{RC} are insensitive to Re for low Σ^* .

Figure 13 shows the cavitation region on an inducer blade for $\Sigma^* = 1.23$ at $Re = 4.81 \times 10^6$ (Figure 13a) and 6.84×10^6 (Figure 13b). For $\Sigma^* = 1.23$, the length of the inducer blade cavitation region at $Re = 6.84 \times 10^6$ is visibly longer

than that at $Re = 4.81 \times 10^6$. Thus, the rotating cavitation onset depends on Re at $\Sigma^* = 1.23$. Tokumasu et al. (2005) performed a numerical analysis of the Re effects on cavitation growth for a hydrofoil. They found that the cavitation region is bigger at a higher Re in liquid oxygen in which the thermal effect is significant. For high Σ^* values, where the thermal effect is significant, as Re increases, the dynamic head ($\frac{1}{2}\rho_l U^2$) in Equation 5 increases, reducing σ_{min} . Thus, increasing Re promotes cavitation region growth, and the rotating cavitation onset occurs at a higher cavitation number. In typical rocket engines, Σ^* (1.5 ~ 30) and Re (1.0×10^7 ~ 10^8) are larger than the tested

Table 3. Test conditions for Reynolds number effects.

| Temperature [K] | Rotational speed [rpm] | Reynolds number | Σ^* |
|-----------------|------------------------|--------------------|-----------------------|
| 297 | 4,500 | 2.30×10^6 | 1.29×10^{-2} |
| 298 | 4,900 | 2.50×10^6 | 1.22×10^{-2} |
| 300.5 | 5,800 | 3.17×10^6 | 1.23×10^{-2} |
| 310 | 4,150 | 2.76×10^6 | 5.33×10^{-2} |
| 315 | 5,000 | 3.52×10^6 | 5.38×10^{-2} |
| 318 | 5,700 | 4.16×10^6 | 5.42×10^{-2} |
| 318 | 4,400 | 3.38×10^6 | 1.04×10^{-1} |
| 321 | 5,200 | 4.21×10^6 | 1.06×10^{-1} |
| 323 | 5,800 | 4.85×10^6 | 1.08×10^{-1} |
| 328 | 4,350 | 3.95×10^6 | 2.57×10^{-1} |
| 330.5 | 4,950 | 4.65×10^6 | 2.57×10^{-1} |
| 333 | 4,700 | 5.56×10^6 | 2.57×10^{-1} |
| 335 | 4,000 | 4.02×10^6 | 5.15×10^{-1} |
| 337.5 | 5,550 | 4.74×10^6 | 5.18×10^{-1} |
| 340 | 5,200 | 5.60×10^6 | 5.16×10^{-1} |
| 341 | 5,450 | 5.94×10^6 | 5.16×10^{-1} |
| 342 | 5,700 | 6.30×10^6 | 5.20×10^{-1} |
| 346.5 | 4,100 | 4.81×10^6 | 1.22 |
| 348 | 4,300 | 5.14×10^6 | 1.26 |
| 350 | 4,700 | 5.75×10^6 | 1.26 |
| 351.5 | 5,100 | 6.36×10^6 | 1.26 |
| 353 | 5,400 | 6.84×10^6 | 1.27 |

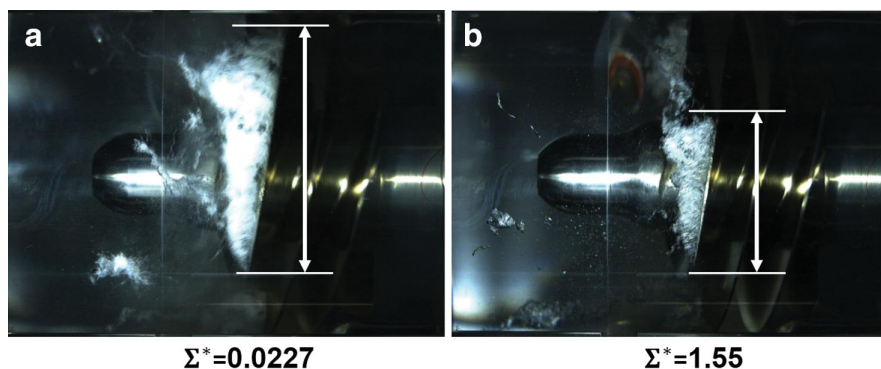


Figure 8. The inducer blade cavitation for $\Sigma^* = 0.0227$ (a) and 1.55 (b) ($\sigma = 0.081$, $\varphi/\varphi_d = 1.0$, $Re = 4.15 \times 10^6$).

conditions. Thus, the effects of Σ^* and Re are expected to be more significant in real operating conditions.

Based on the current results, Figure 1 from Kim and Song (2016) can be explained as follows. Figure 14 shows the combined plots of Figure 1 and Figure 7. In Kim and Song (2016), experiments had been performed by varying Σ^* while maintaining a constant rotational speed of 5,000 rpm. Thus, Re increased from 2.6×10^6 to 6.4×10^6 simultaneously as Σ^* was increased

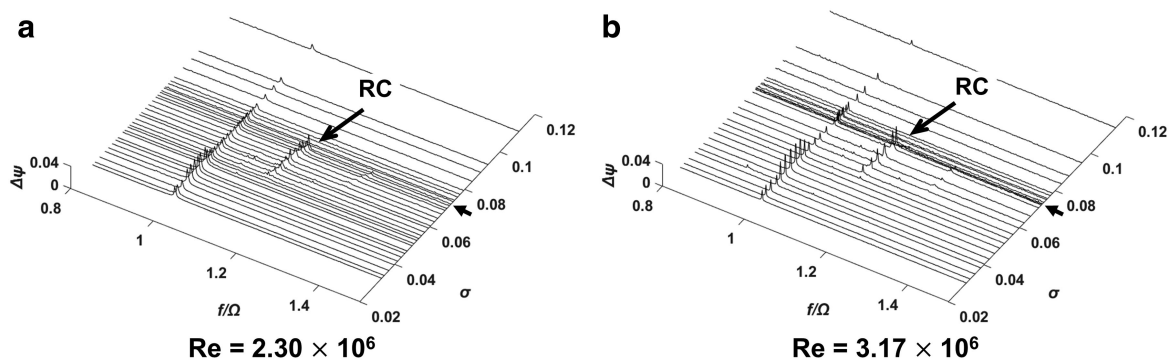


Figure 9. The power spectral density plots of unsteady pressure fluctuations at $\Sigma^* = 0.0125$ and $\varphi/\varphi_d = 1.0$ for $Re = 2.30 \times 10^6$ (a) and $Re = 3.17 \times 10^6$ (b).

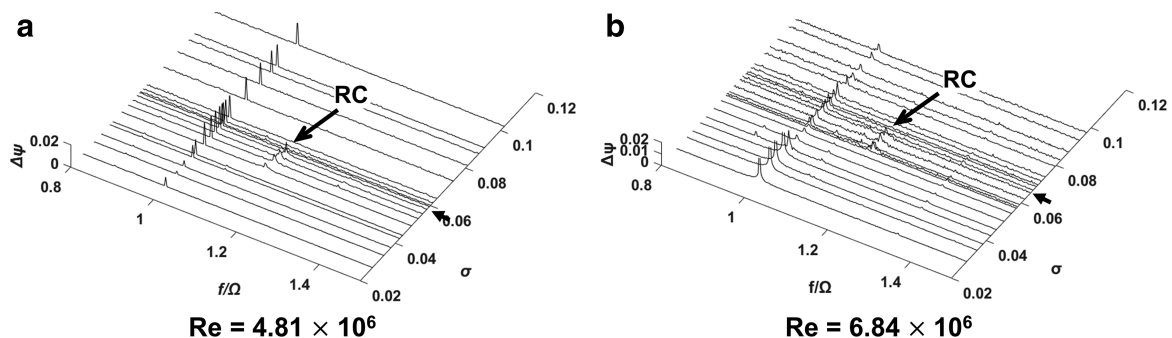


Figure 10. The power spectral density plots of unsteady pressure fluctuations at $\Sigma^* = 1.26$ and $\varphi/\varphi_d = 1.0$ for $Re = 4.81 \times 10^6$ (a) and $Re = 6.84 \times 10^6$ (b).

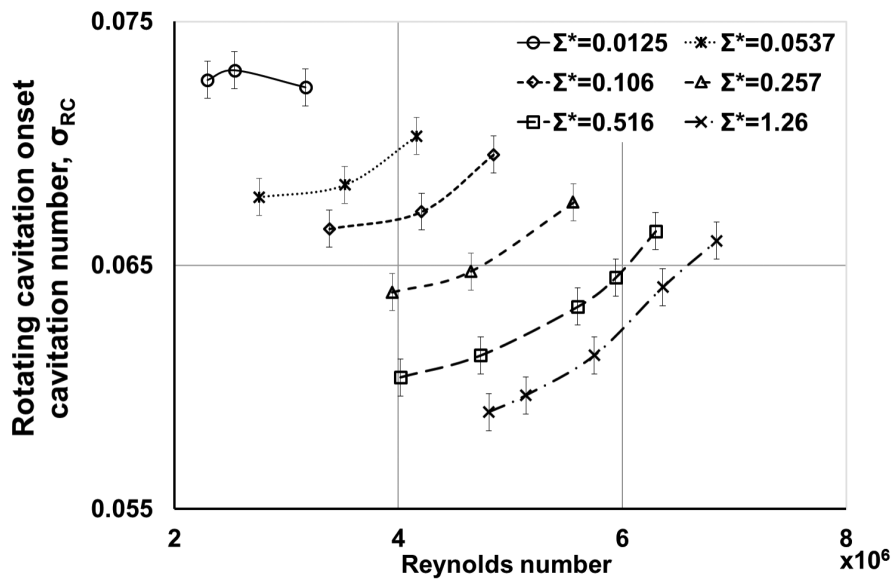


Figure 11. The rotating cavitation onset cavitation number and the critical cavitation number for varying Reynolds numbers and Σ^* at $\varphi/\varphi_d = 1.0$.

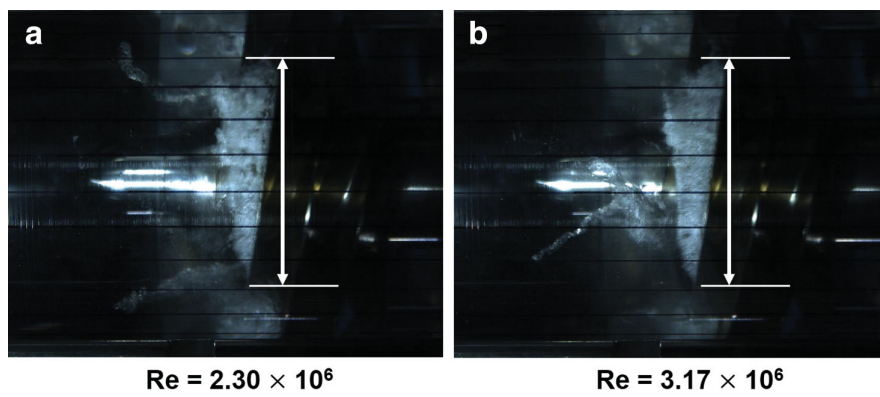


Figure 12. The inducer blade cavitation for $Re = 2.30 \times 10^6$ (a) and 3.17×10^6 (b) ($\sigma = 0.081$, $\varphi/\varphi_d = 1.0$, $\Sigma^* = 0.0125$).

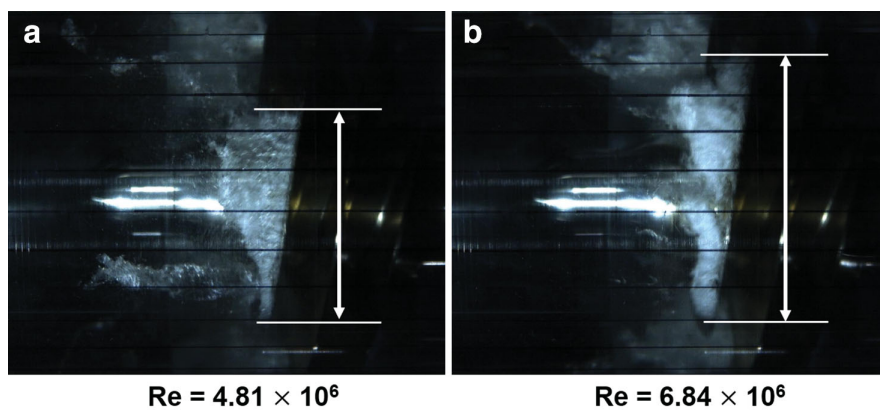


Figure 13. The inducer blade cavitation for $Re = 4.81 \times 10^6$ (a) and 6.84×10^6 (b) ($\sigma = 0.089$, $\varphi/\varphi_d = 1.0$, $\Sigma^* = 1.23$).

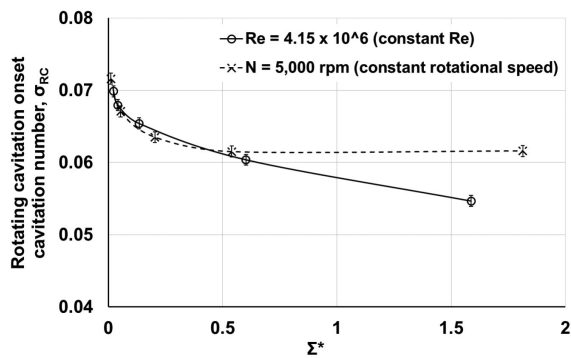


Figure 14. The rotating cavitation onset cavitation number versus the non-dimensional thermal parameter for constant Reynolds number and rotational speed (Kim and Song, 2016) at $\varphi/\varphi_d = 1.0$.

from 0.0116 to 1.80. In Figure 14, σ_{RC} becomes independent of Σ^* for $\Sigma^* > 0.54$ at $N = 5,000$ rpm. On the other hand, σ_{RC} continues to decrease for $\Sigma^* > 0.54$ at $Re = 4.15 \times 10^6$. In the $N = 5,000$ rpm study (Kim and Song 2016), the cavitation suppression effects due to the increase in Σ^* and the cavitation promotion effects due to the increase in Re occurred simultaneously. For $\Sigma^* < 0.54$, the Re effects were weaker, and, thus, σ_{RC} was decreased as Σ^* increased. However, as Σ^* increased further, the Re effects became stronger, essentially cancelling out the Σ^* effects. Thus, σ_{RC} became “seemingly” independent of Σ^* for $0.54 < \Sigma^* < 1.80$ for $N = 5,000$ rpm. However, when Re is kept constant at 4.15×10^6 in the current study, σ_{RC} is decreased as Σ^* increases.

Conclusions

The individual effects of non-dimensional thermal parameter (Σ^*) and Reynolds number (Re) on rotating cavitation onset for a turbopump inducer have been measured in water. The new conclusions from this study are:

1. Increasing the non-dimensional thermal parameter (Σ^*) at a constant Reynolds number (Re) inhibits rotating cavitation onset.
2. Rotating cavitation onset cavitation number (σ_{RC}) increases as the Reynolds number (Re) is increased for Σ^* higher than 0.0537. For Σ^* lower than 0.0125, the rotating cavitation onset is independent of the Reynolds number (Re).
3. Consideration of non-dimensional thermal parameter (Σ^*) alone is insufficient to explain cavitation instability onset. In addition, Reynolds number (Re) has to be considered.

Nomenclature

| | |
|--------------|---|
| A | inducer inlet area |
| c | tip clearance |
| C_{pl} | liquid heat capacity |
| C | characteristic length of inducer |
| D | inducer diameter |
| DB | $r\Omega^{3/2}/\Sigma$ |
| f | frequency (Hz) |
| L | latent heat of the liquid |
| N | rotational speed (rpm) |
| p_{G0} | partial pressure of the non-condensable gas in the bubble |
| p_v | vapor pressure |
| $p_{v,min}$ | minimum vapor pressure |
| Δp_v | vapor pressure depression |
| Q | flow rate |

| | |
|---------------|--|
| r | inducer inlet radius |
| R | bubble radius |
| \bar{R} | non-dimensional bubble radius |
| Re | Reynolds number = $2\rho_1 r \Omega^2 / \mu_l$ |
| S | surface tension |
| t | time |
| T_α | liquid temperature |
| U | tip rotational speed |
| x | distance |
| ρ_1 | liquid density |
| ρ_v | vapor density |
| μ_l | liquid viscosity |
| α_1 | thermal diffusivity of liquid |
| σ | cavitation number, = $(p_1 - p_v) / \frac{1}{2} \rho r^2 \Omega^2$ |
| β | blade tip angle |
| σ_{RC} | rotating cavitation onset cavitation number |
| Φ | flow coefficient, = $Q / Ar \Omega$ |
| Σ | dimensional thermal parameter |
| Σ^* | non-dimensional thermodynamic parameter |
| Ψ | head coefficient, = $(p_2 - p_1) / \frac{1}{2} \rho r^2 \Omega^2$ |
| ψ_0 | head coefficient without cavitation |
| $\Delta \psi$ | unsteady pressure fluctuation coefficient (peak to peak) |
| Ω | inducer rotational speed, rotational frequency (Hz) |

Subscripts

- 1 inlet
- 2 outlet

Funding sources

Financial support from the National Research Foundation of Korea (NSF) (Project Number: 2011-0020908), BK21+ Program, and SNU-IAMD are gratefully acknowledged by the authors.

Competing interests

Junho Kim declares that he has no conflict of interest. Seung Jin Song declares that he has no conflict of interest.

Appendix. Heat transfer analysis of the duct

Following Bergman and Incropera (2011), an expression for the heat flux at the inducer inlet can be inferred from the resistance network as shown in Figure A1 (h_x is the convection heat transfer

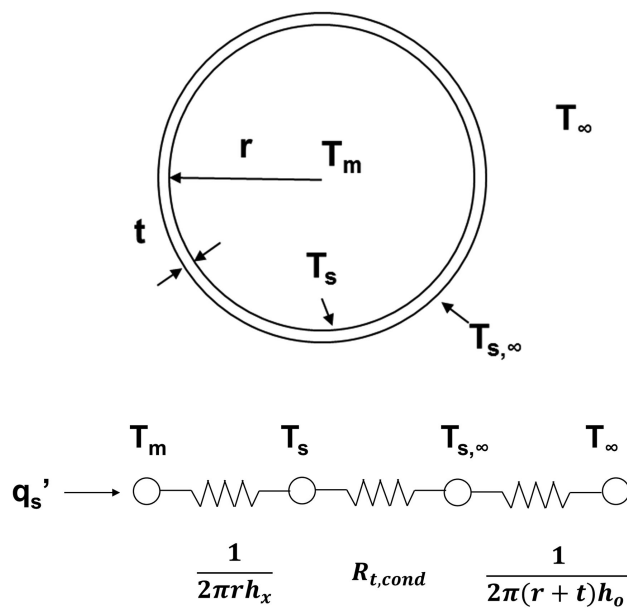


Figure A1. Heat transfer analysis of the duct at the inducer inlet.

coefficient between the water flow and the inner surface of the wall; $R_{t,cond}$ is thermal resistance of cylindrical wall, h_o is natural convection heat transfer coefficient between the duct outer surface and the ambient air, $10 \text{ W/m}^2 \cdot \text{K}$). The following assumptions have been made.

1. The flow is steady with constant properties.
2. Viscous dissipation and pressure variations are negligible.
3. Convection coefficient at outer surface of the duct is uniform.

The heat transfer rate for the duct is expressed as

$$q'_s = \frac{T_m - T_\infty}{[1 / 2\pi r h_x] + [R_{t,cond}] + [1 / 2\pi(r+t)h_o]} = \frac{T_m - T_s}{1 / (2\pi r h_x)} \quad (\text{A1})$$

$$Nu_D = \frac{h_x D}{k} = 0.023 Re_D^{4/5} Pr^{0.3} \quad (\text{A2})$$

With such assumptions and heat transfer equations, the temperature difference between the bulk flow and flow near the wall ranges from 0.042 K (308 K, 6,400 rpm) to 0.091 K (353 K, 5,400 rpm).

References

- Bergman T. L. and Incropera F. P. (2011). Introduction to Heat Transfer, 5th edition. John Wiley & Sons.
- Brennen C. E. (1994). Hydrodynamics of Pumps. Pasadena, California: Concepts ETI, Inc. and Oxford University Press.
- Brennen C. E. (1995). Cavitation and Bubble Dynamics. Concepts ETI, Inc. and Oxford University Press.
- Choi C., Noh J., Kim J., Hong S., and Kim J. (2006). Effects of a bearing strut on the performance of a turbopump inducer. Journal of Propulsion and Power. 22 (6): 1413–1417. <https://doi.org/10.2514/1.19753>.
- Ehrlich D. A. and Murdock J. W. (2015). A dimensionless scaling parameter for thermal effects on cavitation in turbopump inducers. Journal of Fluids Engineering. 137 (4): 041103. <https://doi.org/10.1115/1.4029260>.
- Franc J. P., Boitel G., Riondet M., Jason E., Ramina P., et al. (2010). Thermodynamic effect on a cavitating inducer-part 1: Geometrical similarity of leading edge cavities and cavitation instabilities. Journal of Fluids Engineering. 132 (2): 021303. <https://doi.org/10.1115/1.4001006>.
- Franc J. P., Jason E., Morel P., Rebattet C., and Riondet M. (2001). Visualization of leading edge cavitation in an inducer at different temperatures. Fourth International Symposium on Cavitation, CAV 2001, Pasadena, CA, USA, June 20–23.

- Franc J. P., Rebattet C., and Coulon A. (2004). An experimental investigation of thermal effect in a cavitating inducer. *Journal of Fluids Engineering*. 126 (5): 716–723. <https://doi.org/10.1115/1.1792278>.
- Horiguchi H., Watanabe S., and Tsujimoto Y. (2000). A linear stability analysis of cavitation in a finite blade count impeller. *Journal of Fluids Engineering*. 122 (4): 798–805. <https://doi.org/10.1115/1.1315300>.
- Kikuta K., Yoshida Y., Hashimoto T., Nanri H., Mizuno T., et al. (2009). Influence of rotational speed on thermodynamic effect in a cavitating inducer. *ASME Fluids Engineering Division Summer Meeting, Colorado, USA, August 2–6*. 1: 77–83. <https://doi.org/10.1115/FEDSM2009-78083>.
- Kikuta K., Yoshida Y., Watanabe M., Hashimoto T., Nagaura K., et al. (2008). Thermodynamic effect on cavitation performances and cavitation instabilities in an inducer. *Journal of Fluids Engineering*. 130 (11): 111302. <https://doi.org/10.1115/1.2969426>.
- Kim J. and Song S. J. (2016). Measurement of temperature effects on cavitation in a turbopump inducer. *Journal of Fluids Engineering*. 138 (1): 011304. <https://doi.org/10.1115/1.4030842>.
- Plesset M. and Prosperetti A. (1977). Bubble dynamics and cavitation. *Journal of Fluid Mechanics*. 9: 145–185. <https://doi.org/10.1146/annurev.fl.09.010177.001045>.
- Ruggeri R. S. and Moore R. D. (1969). Method for Prediction of Pump Cavitation Performance for Various Liquids, Liquid Temperatures, and Rotative Speeds. Washington, D.C.: NASA Report. TN-5292.
- Tokumasu T., Sekino Y., and Kamijo K. (2005). The numerical analysis of the effect of flow properties on the thermodynamic effect of cavitation. *Trans. Japan Society for Aeronautical and Space Science*. 47 (156): 146–152. <http://doi.org/10.2322/tjsass.47.146>.
- Torre L., Cervone A., Pasini A., and d'Agostino L. (2011). Experimental characterization of thermal cavitation effects on space rocket axial inducers. *Journal of Fluids Engineering*. 133 (11): 111303. <http://doi.org/10.1115/1.4005257>.
- Tsujimoto Y., Yoshida Y., Maekawa Y., Watanabe S., and Hashimoto T. (1997). Observations of oscillating cavitation of an inducer. *Journal of Fluids Engineering*. 119 (4): 775–781. <http://doi.org/10.1115/1.2819497>.
- Yoshida Y., Sasao Y., Okita K., Hasegawa S., Shimagaki M., et al. (2007). Influence of thermodynamic effect on synchronous rotating cavitation. *Journal of Fluids Engineering*. 129 (7): 871–876. <http://doi.org/10.1115/1.2745838>.
- Yoshida Y., Sasao Y., Watanabe M., Hashimoto T., Iga Y., et al. (2009). Thermodynamic effect on rotating cavitation in an inducer. *Journal of Fluids Engineering*. 131 (9): 091302. <http://doi.org/10.1115/1.3192135>.
- Watanabe S., Furukawa A., and Yoshida Y. (2008). Theoretical analysis of thermodynamic effect on cavitation in cryogenic inducer using singularity method. *International Journal of Rotating Machinery*. 2008: 125678. <http://doi.org/10.1155/2008/125678>.
- Watanabe S., Hidaka T., Horiguchi H., Furukawa A., and Tsujimoto Y. (2007). Analysis of thermodynamic effects on cavitation instabilities. *Journal of Fluids Engineering*. 129 (9): 1123–1130. <http://doi.org/10.1115/1.2754326>.